Tectonophysics 624–625 (2014) 24–31

Contents lists available at ScienceDirect

Tectonophysics

journal homepage: www.elsevier.com/locate/tecto

Remanent magnetization in fresh xenoliths derived from combined demagnetization experiments: Magnetic mineralogy, origin and implications for mantle sources of magnetic anomalies

Fatima Martin-Hernandez [a,b,*], Eric C. Ferré [c], Sarah A. Friedman [c]

[a] Department of Geophysics Universidad Complutense de Madrid, Madrid 28040, Spain
[b] Instituto de Geociencias IGEO (UCM, CSIC), Fac. CC. Físicas, Av. Complutense s/n, 28040 Madrid, Spain
[c] Department of Geology, Southern Illinois University, Carbondale, IL 62901, USA

ARTICLE INFO

Article history:
Received 30 July 2013
Received in revised form 3 April 2014
Accepted 6 April 2014
Available online 15 April 2014

Keywords:
Mantle xenoliths
Magnetic properties
Coercivity spectra
NRM
AF demagnetization

ABSTRACT

Fresh mantle xenoliths represent an exceptional opportunity to directly access Earth's interior. In particular, magnetic signals carried by upper mantle xenoliths may provide the only opportunity to determine the depth of remanent magnetization below the Moho boundary. In recent years, the nature, intensity and magnetic properties of the magnetic signal have been characterized by measurements of the 0020 induced magnetization in hysteresis loops. The natural remanent magnetization (NRM) intensity, despite providing the first indication of the magnetic nature of magnetite inclusions, has not been studied in detail. This study focusses attention on the number of recorded NRM directions and characteristics of the anhysteretic remanent magnetization (ARM) and saturation isothermal remanent magnetization (SIRM) demagnetization spectra. A collection of 17 extremely fresh mantle xenoliths has been subjected to AF demagnetization, characterizing samples with one, two or three populations of remanence carriers, with differing coercivities, that are potential carriers of magnetization at mantle depths.

1. Introduction

Interest in the magnetic properties of mantle materials was sparked by the first Magsat satellite mission. Early works focussed on demagnetization of mantle xenoliths by classical paleomagnetic techniques (Wasilewski, 1987; Wasilewski and Mayhew, 1992; Wasilewski et al., 1979) and continued with correlations between the optical microscopy, compositional analyses of the iron-bearing phases and magnetic properties (Warner and Wasilewski, 1995, 1997).

The magnetic minerals identified in mantle xenoliths were considered to be above their Curie temperature at the equilibration depth, and therefore in a paramagnetic state in situ (Wasilewski and Mayhew, 1992; Wasilewski et al., 1979), until recently (Al-Malabeh et al., 2009; Ferré et al., 2013). However, the re-examination of the magnetic state of the upper mantle leads to new interests in the magnetic mineralogy of this part of the Earth lithosphere (Ferré et al., 2014).

The Natural Remanent Magnetization (NRM) of mantle xenoliths does not represent a remanent magnetization of the mantle but a later Thermomagnetic Remanent Magnetization (TRM) acquired during the eruption process. Therefore the presence of more than one NRM component does not necessary imply the presence of alteration but could be accounted by i) different characteristics of the magnetic carriers and/or ii) multi-stage uplift processes.

This work analyses the Alternating Field (AF) demagnetization of the NRM and two artificially applied laboratory-controlled magnetizations in a collection of 17 extremely fresh mantle xenoliths from two localities, Hawaii and the Massif Central. This work reports new properties of some of the samples reported by Ferré et al. (2013) and samples from the same collection not included in their work.

This paper presents for the first time Zijderveld plots of NRM in mantle xenoliths that allow a correlation between thermal and coercivity spectra of the natural magnetization. The coercivity distribution has been fully additionally characterized by modelling the demagnetization of Anhysteretic Remanent Magnetization (ARM) and Saturation Isothermal Remanent Magnetization (SIRM).

2. Magnetic measurements and samples description

Two suites of petrologically well-studied mantle xenoliths have been analysed for this work. All samples were selected from the interior

* Corresponding author at: Department of Geophysics Universidad Complutense de Madrid, Madrid 28040, Spain.
E-mail address: fatima@ucm.es (F. Martin-Hernandez).

http://dx.doi.org/10.1016/j.tecto.2014.04.006
0040-1951/

part of each xenolith and cut into cubes of 1 cm^3 using non-magnetic saw blades.

Samples include 8 specimens from the Salt Lake crater on Oahu island, Hawaii (USA) (Sen, 1988). Thermobarometry of the garnet-spinel xenoliths in this setting estimates a mean depth of 60 km (Sen et al., 2005). A second selection of pristine xenoliths studied includes 9 specimens from anorogenic intra-plate volcanic rocks presented at the Massif Central (France). These samples have been characterized in major and minor trace elements (Lenoir et al., 2000) and are of particular interest in terms of rock magnetism due to the high S content (Ferré et al., 2013; Lorand et al., 2003). A more detailed description of these samples and their geological framework can be found in Ferré et al. (2013), who importantly found that magnetite is the only significant carrier of remanent magnetization in these samples.

Low field magnetic susceptibility has been measured in a KLY4S susceptibility bridge, manufactured by AGICO, in all the samples.

The Natural Remanent Magnetization (NRM) of all samples has been demagnetized by the Alternating Field (AF) protocol in a 2G-755 Superconducting Magnetometer. The NRM vector has been cleaned by this non-destructive method by using 1 mT steps up to 10 mT and further 10 mT steps up to a 120 mT (e.g., Butler, 1992; Tauxe, 2010). Magnetization vector directions have been graphically inspected by projecting the NRM into two-dimensional projections (Zijderveld plots) in order to check for the number of magnetizations registered in the xenoliths (Zijderveld, 1967).

After complete removal of the NRM by AF demagnetization an Anhysteretic Remanent Magnetization (ARM) of 100 μT DC field and 100 mT peak alternating field has been applied along the samples' coordinate Z direction to some selected samples from the two localities (Collinson, 1983; Stacey and Banerjee, 1974). The artificial ARM vector has been further demagnetized by AF magnetic cleaning following the same demagnetization steps used for the NRM. ARM magnetization and AF demagnetization has been applied and measured also in a 2G-755 Superconducting Magnetometer.

A Saturating Isothermal Remanent Magnetization (SIRM), acquired in 2 T, has been further applied to some selected samples with a M2T-1 pulse magnetizer manufactured by Ferronato (Collinson, 1983; Stacey and Banerjee, 1974). The SIRM acquired has been AF demagnetized in a 2G-755 Superconducting Magnetometer with the previously described demagnetization protocol.

The magnetic particles have also been characterized by analysing the ARM and SIRM coercivity spectra, after converting the AF demagnetization curves into the corresponding remanence acquisition curve in order to estimate the coercivity of each magnetic population. For both artificial fields the coercivity spectra have been fitted into a series of log-Gaussian distribution curves following the procedure outlined by Kruiver et al. (2001). The median destructive field ($B_{1/2}$) and dispersion parameter (DP) of each coercivity component for ARM and SIRM have been correlated to the number of NRM components at each sample.

3. Results

3.1. NRM analysis

Initial values of the NRM for the 17 studied xenoliths are compiled in Table 1. Values are of the same order of magnitude as data already reported for mantle xenoliths (Ferré et al., 2014; Friedman et al., sumitted for publication; Warner and Wasilewski, 1995) with intensity ranging from 1.36×10^{-4} Am^2/kg recorded by sample LI2 to 6.51×10^{-7} Am^2/kg in sample SAL10 (Table 1).

The AF demagnetization analysis of the NRM vector shows three different behaviours independently of the setting (Table 1). Eight samples display a single NRM component over the full coercivity range (Fig. 1a and Fig. 1b). Five presented two separate NRM components, the first one demagnetizing at a maximum AF peak field 10–15 mT and a second component that demagnetizes at a maximum field higher than 120 mT with almost no overlap between them (Fig. 1c and d). Four samples also display two NRM components with overlapping coercivity spectra (Fig. 1e and f). One sample (RP3) exhibits noisy behaviour above 40 mT and does not demagnetize completely (Fig. 1g).

Fig. 2 shows the normalized NRM decay plot for all the studied xenoliths. The demagnetization curve in samples where more than one NRM component has been observed is computed following the Vector Difference Magnitude (VDM) procedure (Gee et al., 1993). Demagnetization plot is very similar in both settings in terms of shape of the demagnetization plot. The majority of the Hawaiian samples have a lower median destructive field (MDF), than the majority of the Massif Central samples. MDF is the field necessary to demagnetize half of the initial NRM (Dunlop and Özdemir, 1997). The median destructive field ranges from 5 to 30 mT in Hawaiian samples (Fig. 2a) and from 10 to 40 mT in samples from the Massif Central (Fig. 2b), reflecting a slightly harder remanence in the second location.

3.2. ARM demagnetization by AF

A weak ARM with a maximum DC field of 100 μT has been applied to four samples from the Hawaiian collection and three samples from the

Table 1
Sample location, NRM intensity of all studied sample and number of identified components (ov. meaning that the number of components presents a certain degree of coercivity overlapping), low field mass susceptibility, ARM intensity and SIRM intensity of selected samples. Number of NRM components with * indicates samples for which there is a component along the sample coordinate either at low coercivities (suspected to be acquired in the cutting process) or at high coercivities (suspected to be a GRM).

	Sample name	Mass [g]	NRM [Am^2kg^{-1}]	NRM components	K [m^3/kg]	ARM [Am^2kg^{-1}]	SIRM [Am^2kg^{-1}]
Hawaii	SAL3	2.96	1.60×10^{-6}	2 ov.	1.79×10^{-6}	1.72×10^{-6}	2.63×10^{-5}
	SAL4	3.72	1.77×10^{-5}	2	2.04×10^{-6}	1.26×10^{-5}	4.27×10^{-4}
	SAL6−25	0.66	5.02×10^{-5}	1	1.66×10^{-6}		
	SAL6−25b	0.75	2.64×10^{-5}	1	1.80 10^{-6}		
	SAL10	2.54	6.51×10^{-7}	2	2.06×10^{-6}	9.85×10^{-6}	
	SAL16	1.34	1.62×10^{-6}	2	1.63×10^{-6}		
	SAL18	2.31	1.40×10^{-6}	2 ov.	1.85×10^{-6}	2.02×10^{-6}	2.52×10^{-5}
	SAL20	2.26	8.95×10^{-6}	1	1.93×10^{-6}		
Massif Central	BC2A	2.85	4.49×10^{-6}	2	2.11×10^{-6}	1.21×10^{-5}	1.31×10^{-3}
	EG01	3.48	4.82×10^{-6}	1	1.15×10^{-6}		
	LI2	2.66	1.36×10^{-4}	1*	2.29×10^{-6}		
	MP1A	3.49	3.50×10^{-6}	1	1.79×10^{-6}		
	NSB1	3.44	1.49×10^{-5}	2 ov.	2.03×10^{-6}		
	PG43	2.59	2.09×10^{-6}	1	1.86×10^{-6}	8.78×10^{-6}	6.28×10^{-4}
	PT3	2.92	1.90×10^{-6}	2 ov.	1.77×10^{-6}		
	RP3	2.56	2.18×10^{-6}	2*	1.61×10^{-6}	1.02×10^{-6}	2.69×10^{-4}
	SMP	2.56	5.52×10^{-4}	1	2.80×10^{-6}		

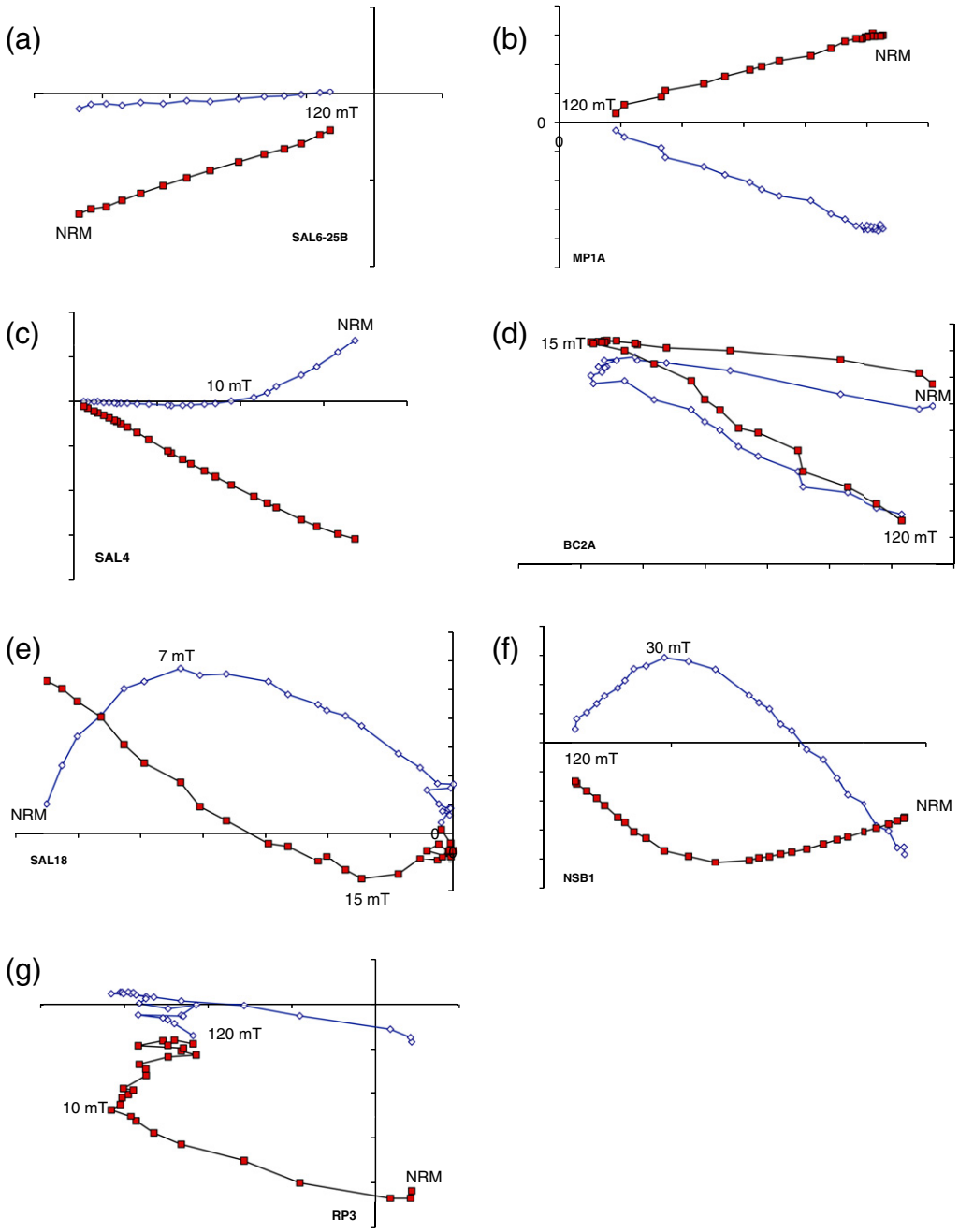

Fig. 1. Typical Zijderveld plots in sample coordinates of the AF demagnetization of NRM vector in mantle xenoliths from Hawaii (a, c and e) and Massif Central (b, d, f and g).

Massif Central set (Table 1). In all samples ARM intensity has the same order of magnitude as the corresponding NRM, with the exception of samples BC2A and SAL10 that have a stronger ARM maximum intensity (Table 1).

The ARM normalized decay plot shows a MDF raging between 25 and 38 mT in samples from Hawaii (Fig. 3a) and between 22 and 34 mT in samples from the Massif Central (Fig. 3b). Differences in the MDF of ARM are indicative of differences in the grain size of magnetic particles due to the strong influence of grain size on AF demagnetization spectra of ARM (e.g., Dunlop and Özdemir, 1997). Sample RP3 displayed an increase in magnetization after the 40 mT AF demagnetization step (Fig. 3b) with an associated NRM direction along the sample's Z direction, which might suggest the acquisition of a Gyro-remanent Magnetization (GRM) in the sample (Stephenson, 1980). The ARM gradient as a function of applied field shows a fairly symmetric distribution of coercivities (Fig. 3c and d). Most specimens show very similar gradients with variations on the intensity and a unique maximum centred around 10–25 mT and varying mainly in peak intensity, suggesting similar characteristics in size of the magnetic carriers. The two exceptions are sample BC2A that displays two local maxima at 2–5 mT and 40 mT and sample RP3 that acquired a GRM after 40 mT of AF field (Fig. 3d).

The gradient of the ARM demagnetization curve has been modelled using multiple log-Gaussian distributions with the method and software presented by Kruiver et al. (2001). All samples could be modelled with two coercivity distributions (Fig. 3e and f). This comprises a low coercivity component with low intensity and a mean median destructive field of

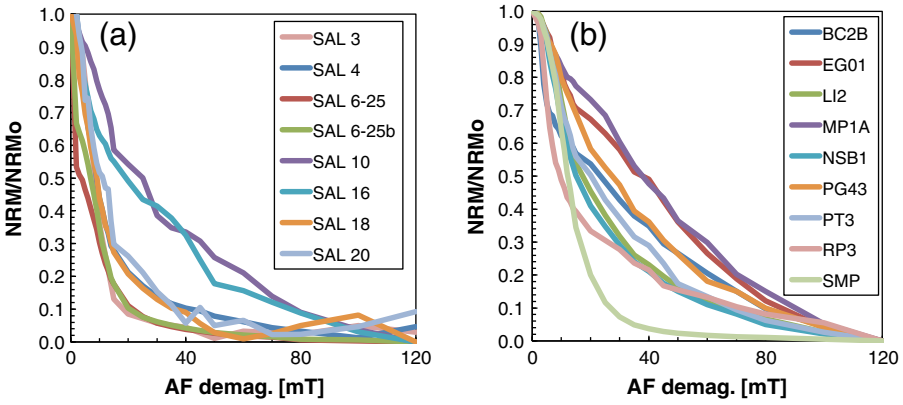

Fig. 2. Normalized AF demagnetization decay plot of the NRM of samples from Hawaii (a) and Massif Central (b). For samples with more than one NRM component, the decay plot has been computed following the Vector Difference Magnitude (VDM) procedure (Gee et al., 1993).

3.88 ± 0.48 mT and a mean DP of 2.87 ± 0.19 mT, and a second component that dominates the signal with a median destructive field of 24.3 ± 3.4 mT and a mean DP of 1.896 ± 0.046 mT (Table 2).

3.3. SIRM demagnetization by AF

A saturating IRM of 2 T has been applied to six samples from this study in order to study the magnetic behaviour of the harder magnetic fraction. Maximum intensity of the acquired remanence ranges from 1.3×10^{-3} [Am^2kg^{-1}] to 2.6×10^{-5} [Am^2kg^{-1}] (Table 1).

The AF demagnetization of the SIRM applied to the samples shows a very coherent median destructive field with values ranging between 21 mT and 44 mT (Fig. 4) with the exception of sample PG43 (Fig. 4b).

The gradient of the SIRM demagnetization curve is however, more complex than the analogous ARM gradient. For all xenoliths, the SIRM demagnetization spectra are unimodal, but the field at which the spectrum peaks varies from 8 mT for sample SAL 4 to values higher than the maximum applied field (Fig. 4c and d).

Mathematical modelling of the SIRM demagnetization curves reveals two types of coercivity distributions (Table 2). All samples exhibit, i) one low coercivity component with a $B_{1/2}$ mean value of 5.4 ± 1.1 mT and a DP of 2.09 ± 0.10 mT and ii) a medium coercivity component with $B_{1/2}$ mean value of 25.8 ± 5.4 mT and a DP of 2.042 ± 0.080 mT (Table 2 and Fig. 4e). Six samples showed an additional high coercivity component peak below the maximum available field and it is characterized by an extrapolated $B_{1/2}$ = 79 ± 21 mT and DP = 1.80 ± 0.18 mT (Table 2 and Fig. 4f).

4. Discussion

Magnetite has been identified as the main carrier of NRM in mantle xenoliths by thermomagnetic curves (Warner and Wasilewski, 1997), thermal demagnetization of NRM (Warner and Wasilewski, 1995) or, in samples from this collection, identification of the magnetite Verwey transition by low temperature magnetization curves (Ferré et al., 2013). Additionally, high concentrations of S have been identified in mantle xenoliths (Guo et al., 1999; Lenoir et al., 2000) and the low temperature pyrrhotite transition has also been detected in mantle xenoliths (Ferré et al., 2013).

Fig. 5 shows direct comparison of AF demagnetization of the ARM and NRM curves can be used as a diagnosis for the physical mechanism of acquisition of remanence in natural samples (see Dunlop and Özdemir, 1997, for a detailed explanation). This comparison is better applied in samples where one single NRM component is present (Fig. 5b and Table 1). The NRM and ARM are broadly similar, which is consistent with the interpretation of NRM as TRM (Ferré et al., 2013).

The ARM demagnetization plot can be, therefore be used as a grain size estimator, assuming a weak field ARM can be considered an analog of a weak field TRM (Dunlop and Özdemir, 1997). The AF demagnetization curves of a weak field ARM can be therefore compared with AF demagnetization of TRM of grain size controlled fractions of magnetite (Argyle and Dunlop, 1990). The median destructive field of the ARM demagnetization coincides with the PSD grain to SD grain size for pure magnetite at both sites, although slightly larger in the samples from the Massif Central (Fig. 2).

Additionally, an examination of the SIRM demagnetization helps inferring information about high coercivity magnetic phases. In particular, the SIRM demagnetization curve for sample RP3 plots well above its ARM demagnetization curve. Furthermore, spurious magnetization acquired upon high field AF demagnetization of the ARM suggests acquisition of a GRM (Fig. 5). A twin sample from this location has been previously analysed by Lorand et al. (2003), who report the highest S content in mantle xenoliths yet found, with a value of 600 ppm. The increase in the ARM demagnetization plot (Fig. 3) and high S content suggest pyrrhotite might be present in the samples (Thomson, 1990). However, its contribution to the NRM is still underdetermined (Ferré et al., 2013).

In previous studies, magnetic properties focussed on hysteresis-derived parameters and have been determined only in those samples where only one NRM component has been observed (Ferré et al., 2013). However, a deeper analysis into the Zijderveld plots reveals that two NRM components are not necessarily correlated to high coercivity phases, but rather to low coercivity grains with different domain state, grain size or stoichiometry (Figs. 3 and 4). The number of NRM components correlates well with the number of ARM coercivity distributions that fit the ARM gradient (Fig. 3 and Table 2) at least in the samples analysed with AF demagnetization.

SIRM maximum values can be still considered relatively weak (Table 2). The maximum value of 1.3×10^{-3} Am/kg corresponds to a magnetization of about 4 A/m (assuming a sample density of just over 3000 kg/m^3). If the carriers are SD magnetite, for which the saturation remanence is 240 kA/m, this implies a magnetite content of only 0.0016%. TRM acquired in a field of 50 μT for such grains is about 5 kA/m (Dunlop and Özdemir, 1997). NRMs of these samples are not high enough to represent sources of substantial magnetic anomalies at satellite altitudes. However, they indicate the potential for otherwise similar mantle rocks that have been metasomatized under similar conditions, but somewhat more strongly, to contain higher concentrations of magnetite and thereby carry sufficient magnetization to produce observable anomalies, if present in large volumes.

Fig. 6 compares the MDF of the coercivity components defined by ARM and SIRM demagnetization curves. The correlation between MDFs of the ARM and SIRM for the low and medium coercivity magnetic

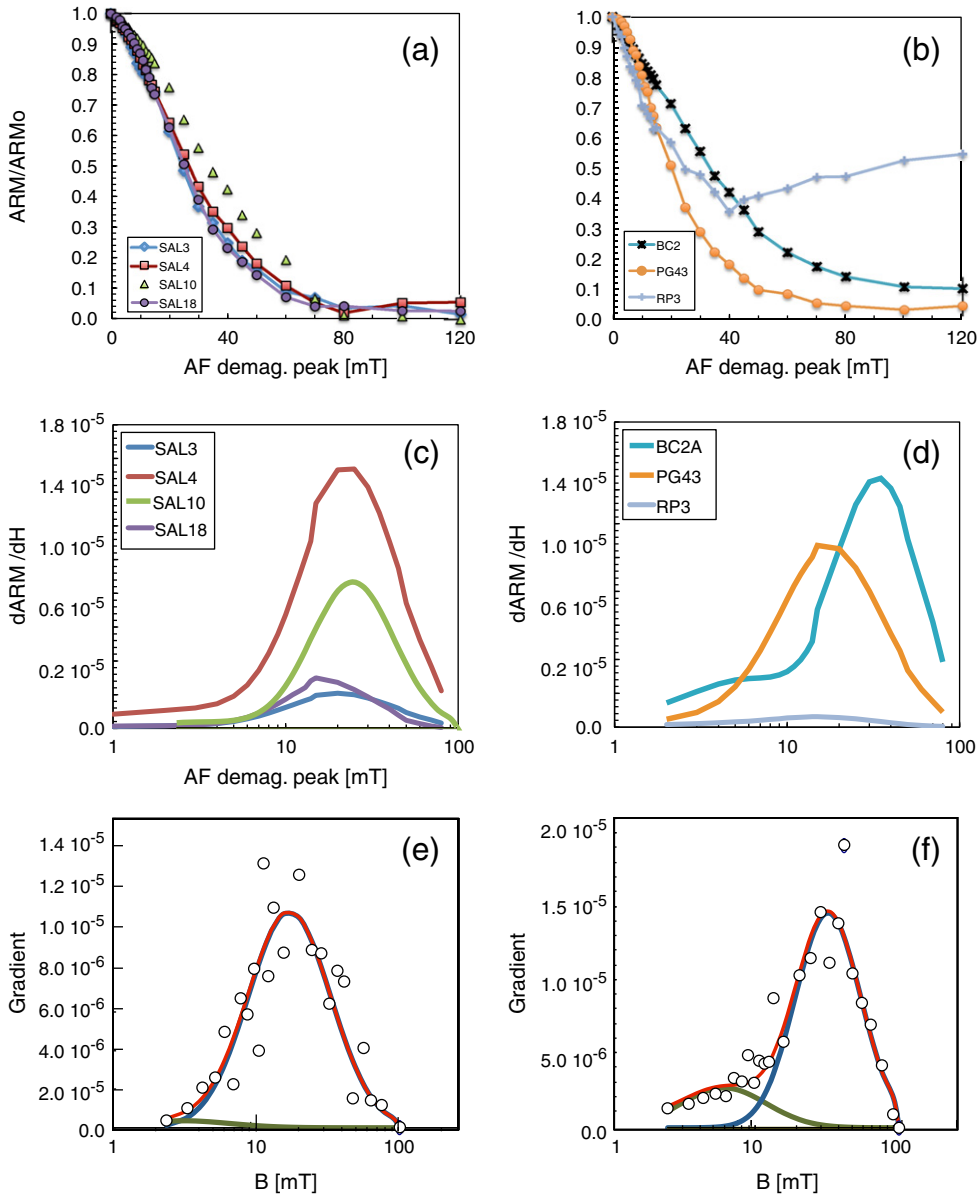

Fig. 3. Analysis of the AF demagnetization of an ARM on selected samples. Normalized AF demagnetization decay plot of a 100 μT DC field with a 100 mT peak field in samples from Hawaii (a) and Massif Central (b), differential magnetization as a function of AF demagnetization peak in samples from Hawaii (c) and Massif Central (d) and modelled coercivity spectra derived from the AF demagnetized ARM using the method of Kruiver et al. (2001) showing representative samples with one main component illustrated by sample PG43 (e) and two components illustrated by sample BC2A (f).

Table 2
Summary of the main parameters of the coercivity spectral analysis of the ARM and SIRM where $B_{1/2}$ is the fitted value of the median destructive field and DP is the dispersion parameter (in mT). For each component, the arithmetic mean and the Standard Error of the Mean (SEM) are computed.

	ARM						SIRM								
	ARM_1	$B_{1/2}$	SD	ARM_2	$B_{1/2}$	SD	$SIRM_1$	$B_{1/2}$	SD	$SIRM_2$	$B_{1/2}$	SD	$SIRM_3$	$B_{1/2}$	SD
SAL3	1.2×10^{-7}	3.16	3.16	1.6×10^{-6}	22.39	2.04	1.8×10^{-6}	3.98	1.78	1.1×10^{-5}	12.59	1.778	1.3×10^{-5}	50	2.09
SAL4	2.0×10^{-6}	3.16	3.16	1.1×10^{-5}	25.12	1.91	5.0×10^{-5}	6.31	2	3.3×10^{-4}	39.81	2.239	1.2×10^{-3}	40	2.2
SAL10	7.0×10^{-7}	3.2	3.2	9.0×10^{-6}	28.2	1.8									
SAL18	3.8×10^{-7}	3.16	3.16	4.3×10^{-6}	21.38	1.78	7.0×10^{-6}	3.16	2	3.5×10^{-5}	17.78	1.995	1.1×10^{-5}	50	1
BC2A	2.0×10^{-6}	6.31	2.04	9.0×10^{-6}	36.3	1.74	1.0×10^{-5}	10	2	2.4×10^{-4}	44.67	1.862	1.0×10^{-3}	48	1.9
PG43	4.0×10^{-7}	3.16	2.24	8.0×10^{-6}	19.05	2	4.0×10^{-5}	5.62	2.24	4.5×10^{-4}	17.78	2.138	1.4×10^{-4}	126	1.58
RP3	6.0×10^{-7}	5.01	3.16	1.0×10^{-6}	17.78	2	8.0×10^{-6}	3.16	2.51	1.0×10^{-4}	22.39	2.239	6.0×10^{-4}	158	2
mean	$\mathbf{8.9 \times 10^{-7}}$	**3.88**	**2.87**	$\mathbf{6.3 \times 10^{-6}}$	**24.3**	**1.896**	$\mathbf{1.95 \times 10^{-5}}$	**5.4**	**2.09**	$\mathbf{1.94 \times 10^{-4}}$	**25.8**	**2.042**	$\mathbf{4.9 \times 10^{-4}}$	**79**	**1.80**
SEM	$\mathbf{3.0 \times 10^{-8}}$	**0.48**	**0.19**	$\mathbf{1.5 \times 10^{-6}}$	**2.4**	**0.046**	$\mathbf{8.3 \times 10^{-6}}$	**1.1**	**0.10**	$\mathbf{7.2 \times 10^{-5}}$	**5.4**	**0.080**	$\mathbf{2.1 \times 10^{-4}}$	**21**	**0.18**

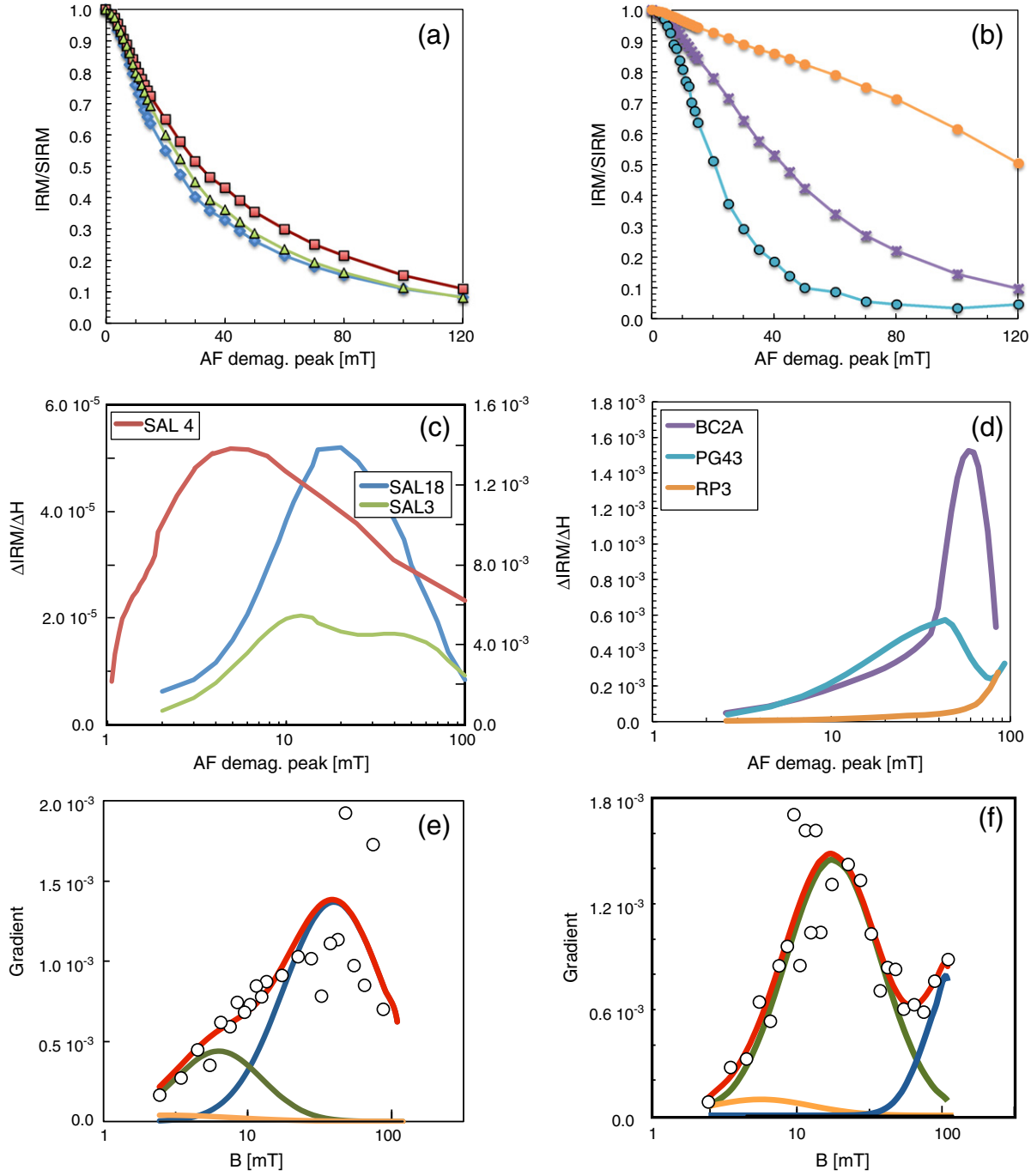

Fig. 4. Analysis of the AF demagnetization of an SIRM on selected samples. Normalized AF demagnetization decay plot of SIRM acquired in 2 T in samples from Hawaii (a) and Massif Central (b), differential magnetization as a function of AF demagnetization peak in samples from Hawaii (c) and Massif Central (d) and modelled coercivity spectra derived from the AF demagnetized SIRM by means of Kruiver et al. (2001) showing representative samples with two main components illustrated by sample SAL4 (e) and three components illustrated by sample PB43 (f).

carriers reveals two distinct groups. Based on theoretical simulations of Heslop et al. (2004), the low-coercivity component, of low SIRM intensity and well-constrained dispersion parameter and very small median destructive field may be attributable to local-interaction field and thermal relaxation. More sophisticated theoretical models of the coercivity distribution include this component into the theoretical function of the main coercivity distribution of the IRM curve (Egli, 2004). However, in this study, no empirical experiment can be carried out in order to distinguish an interaction/thermal activation effect from the presence of a physical low-coercivity magnetic population.

The coercivity distribution has a range of median destructive fields of the ARM from 17.78 to 36.30 mT and the MDF of SIRM ranges from 12.54 to 44.67 mT (Table 2). The correlation between ARM and SIRM coercivity components suggests a non-unique grain size distribution of magnetic particles in the upper mantle.

5. Conclusions

AF demagnetization of NRM in mantle xenoliths shows a complex behaviour with samples that display i) one single component,

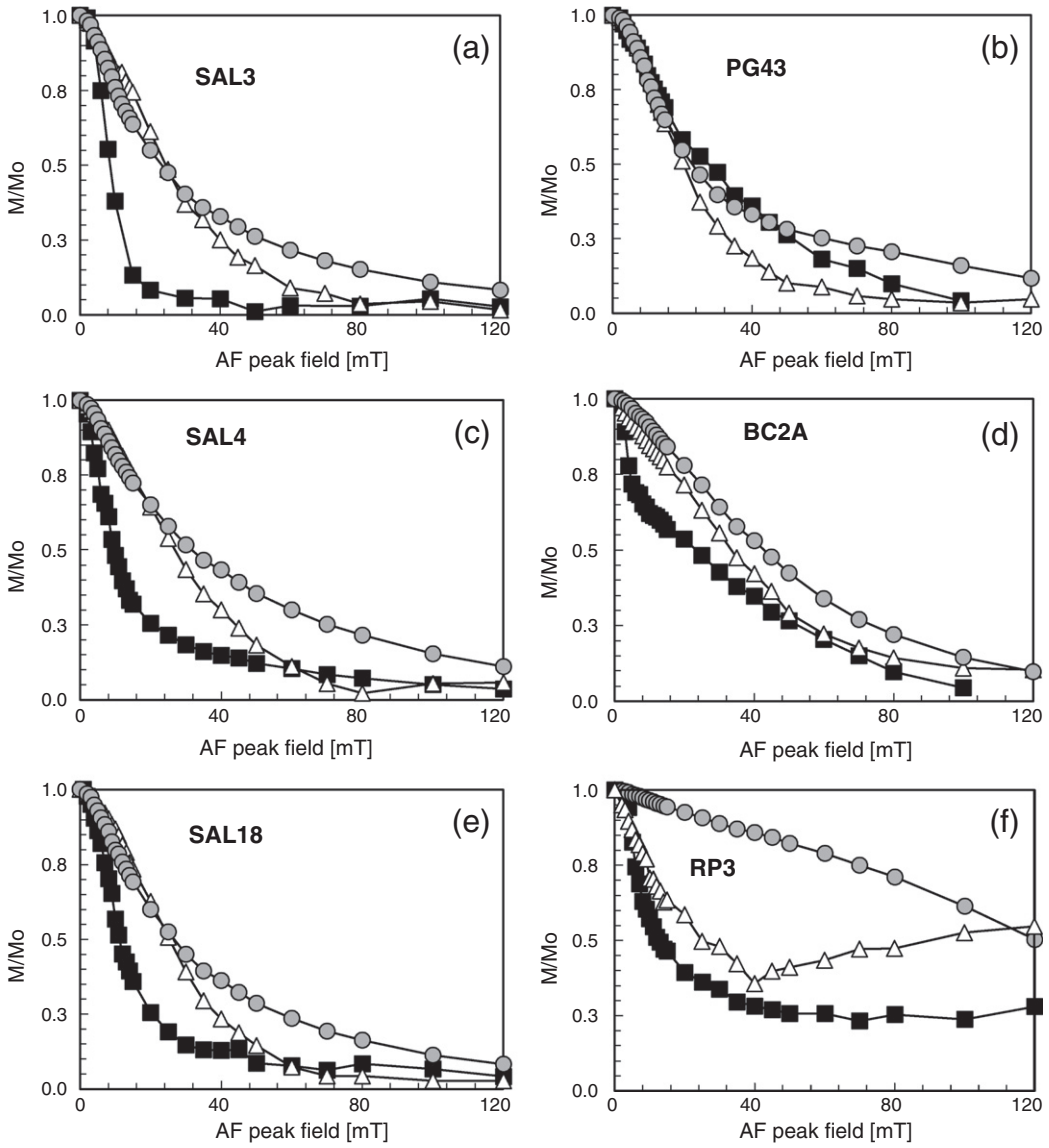

Fig. 5. Comparison between NRM demagnetization curve and artificial ARM and SIRM demagnetization plots in samples from Hawaii (a, c and e) and Massif Central (b, d and f). Black squares correspond to the NRM demagnetization curve, open triangles correspond to the ARM demagnetization curve and grey circles to the SIRM demagnetization curve.

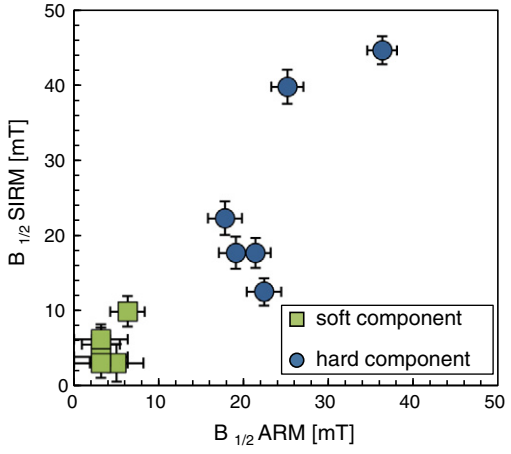

Fig. 6. Relationship between the MDF of the "soft" and "hard" components of the analysed samples modelled coercivity spectra for AF demagnetization of ARM and SIRM. The error bar is given by the corresponding DP of the coercivity spectra according to Kruiver et al. (2001).

ii) two isolated components, iii) two overlapping components and iv) three components. Comparison of the NRM and ARM demagnetization decay plots confirms the TRM origin of the natural remanence in mantle xenoliths.

A deeper analysis of the AF demagnetization of ARM and numerical values of the median destructive field suggests a PSD to SD size of the magnetic particles.

AF demagnetization and further modelling of ARM and SIRM shows the presence of one to two different coercivity distributions that dominate the remanence in samples where also two components are present in the NRM.

Additionally, the AF demagnetization of some samples suggests the presence of a GRM that would be attributed to pyrrhotite.

NRMs of these samples are not high enough to represent sources of substantial magnetic anomalies at satellite altitudes. However, they indicate the potential for otherwise similar mantle rocks that have been metasomatized under similar conditions, but somewhat more strongly, to contain higher concentrations of magnetite and thereby carry sufficient magnetization to produce observable anomalies, if present in large volumes.

Acknowledgments

Prof. J.J. Villalaín is acknowledged for providing access to the cryogenic magnetometer at the Burgos University. We thank A. Tommasi and O. Alard for providing both Hawai'i and Massif Central samples. The manuscript has benefit from detailed revision and proofreading of David Clark and two anonymous reviewers. This research has been partially supported by the Ramón y Cajal reseach program to FMH.

References

Al-Malabeh, A.T., El-Hasan, Lataifeh, M., 2009. Petrochemical, petrographic and magnetic characteristics of spinel lherzolite mantle xenoliths from Jabal Remah Volcano, Jordan. Am. J. Appl. Sci. 6, 1308–1312.

Argyle, K.S., Dunlop, D.J., 1990. Low-temperature and high-temperature hysteresis of small multidomain magnetites (215–540 nm). J. Geophys. Res. B: Solid Earth 95, 7069–7083.

Butler, R., 1992. Paleomagnetism. Blackwell Scientific, Cambridge.

Collinson, D.W., 1983. Magnetic Cleaning Techniques, Methods in Rock and Paleomagnetism: Techniques and Instrumentation. Chapman and Hall, New York pp. 308–317.

Dunlop, D.J., Özdemir, Ö., 1997. Rock Magnetism: Fundamentals and Frontiers. Cambridge University Press, Cambridge.

Egli, R., 2004. Characterization of individual rock magnetic components by analysis of remanence curves. 3. Bacterial magnetite and natural processes in lakes. Physics and Chemistry of the Earth, Parts A/B/C 29 (13–14), 869–884.

Ferré, E.C., Friedman, S.A., Martín-Hernández, F., Feinberg, J.M., Conder, J.A., Ionov, D.A., 2013. The magnetism of mantle xenoliths and potential implications for sub-Moho magnetic sources. Geophys. Res. Lett. 40 (1), 105–110.

Ferré, E.C., Friedman, S.A., Martín-Hernández, F., Feinberg, J.M., Till, J.L., Ionov, D.A., Conder, J.A., 2014. Eight good reasons why the uppermost mantle could be magnetic. Tectonophysics 624-625, 3–14.

Friedman, S.A., Ferré, E.C., Demory, F., Martín-Hernández, F., Conder, J.A., Rochette, P., 2014n. Craton vs. rift uppermost mantle contributions to magnetic anomalies in the United States interior. Tectonophysics 624-625, 15–23.

Gee, J., Staudigel, H., Tauxe, L., Pick, T., Gallet, Y., 1993. Magnetization of the La Palma seamount series: implications for seamount paleopoles. J. Geophys. Res. B: Solid Earth 98 (11,743–711,767).

Guo, J., Griffin, W.L., O'Reilly, S.Y., 1999. Geochemistry and origin of sulphide minerals in mantle xenoliths: Qilin, Southeastern China. J. Petrol. 40, 1125–1149.

Heslop, D., McIntosh, G., Dekkers, M.J., 2004. Using time- and temperature-dependent Preisach models to investigate the limitations of modelling isothermal remanent magnetization acquisition curves with cumulative log Gaussian functions. Geophys. J. Int. 157 (1), 55–63.

Kruiver, P.P., Dekkers, M.J., Heslop, D., 2001. Quantification of magnetic coercivity components by the analysis of acquisition curves of isothermal remanent magnetisation. Earth Planet. Sci. Lett. 189, 269–276.

Lenoir, X., Garrido, C.J., Bodinier, J.-L., Dautria, J.-M., 2000. Contrasting lithospheric mantle domains beneath the Massif Central (France) revealed by geochemistry of peridotite xenoliths. Earth Planet. Sci. Lett. 181, 359–375.

Lorand, J.-P., Alard, O., Luguet, A., Keays, R.R., 2003. Sulfur and selenium systematics of the subcontinental lithospheric mantle: inferences from the Massif Central xenolith suite (France). Geochim. Cosmochim. Acta 67, 4137–4151.

Sen, G., 1988. Petrogenesis of spinel lherzolite and pyroxenite suite xenoliths from the Koolau shield, Oahu, Hawaii: implications for petrology of the post-eruptive lithosphere beneath Oahu. Contrib. Mineral. Petrol. 100, 61–91.

Sen, G., Keshav, S., Bizimis, M., 2005. Hawaiian mantle xenoliths and magmas: composition and thermal character of the lithosphere. Am. Mineral. 90, 871–887.

Stacey, F.D., Banerjee, S.K., 1974. The Physical Principles of Rock Magnetism. Elsevier, Amsterdam.

Stephenson, A., 1980. Gyromagnetism and the remanence acquired by a rotating rock in an alternating field. Nature 284, 48–49.

Tauxe, L., 2010. Essentials of Paleomagnetism. University of California Press.

Thomson, G.F., 1990. The anomalous demagnetization of pyrrhotite. Geophys. J. Int. 103, 425–430.

Warner, R.D., Wasilewski, P.J., 1995. Magnetic petrology of lower crust and upper mantle xenoliths from McMurdo Sound, Antarctica. Tectonophysics 249, 69–92.

Warner, R.D., Wasilewski, P.J., 1997. Magnetic petrology of arc xenoliths from Japan and Aleutian Islands. J. Geophys. Res. 102, 20225–20243.

Wasilewski, P.J., 1987. Magnetic properties of mantle xenoliths and the magnetic character of the crust-mantle boundary. In: Nixon, P.H. (Ed.), Mantle Xenoliths. John Wiley & Sons, New York, pp. 577–588.

Wasilewski, P.J., Mayhew, M.A., 1992. The Moho as a magnetic boundary revisited. Geophys. Res. Lett. 19, 2259–2262.

Wasilewski, P.J., Thomas, H.H., Mayhew, M.A., 1979. The Moho as a magnetic boundary. Geophys. Res. Lett. 6, 541–544.

Zijderveld, J.D.A., 1967. A. C. demagnetization of rocks: analysis of results. In: Collinson, D. W., Creer, K.M., Runcorn, S.K. (Eds.), Methods in Palaeomagnetism. Elsevier, Amsterdam, New York, pp. 254–286.